Journal of
Composites Science

MDPI

Article

Descriptor–Response Analysis of CO_2 Adsorption and Activation on Cu_nSc Nanoclusters Using r^{2}SCAN-3c Calculations

Katherine Liset Ortiz Paternina [1,*], Rodrigo Ortega-Toro [2] and Joaquín Hernández Fernández [1,3,4,*]

[1] Chemistry Program, Department of Natural and Exact Sciences, San Pablo Campus, Universidad de Cartagena, Cartagena de Indias D.T. y C., Cartagena 130015, Colombia
[2] Food Packaging and Shelf-Life Research Group (FP&SL), Food Engineering Program, University of Cartagena, Cartagena de Indias 130015, Colombia
[3] Department of Natural and Exact Science, Universidad de la Costa, Barranquilla 080002, Colombia
[4] Grupo de Investigación GIA, Fundacion Universitaria Tecnologico Comfenalco, Cr 44 D N 30A, 91, Cartagena 130015, Colombia
* Correspondence: kortizp1@unicartagena.edu.co (K.L.O.P.); jhernandezf@unicartagena.edu.co (J.H.F.)

Abstract

This study analyzed the initial adsorption and activation of CO_2 on bimetallic Cu_nSc nanoclusters, with n = 3–7, using DFT calculations in ORCA with the r^{2}SCAN-3c method. A total of 20 bare clusters and their corresponding Cu_nSc–CO_2 complexes were investigated, considering four structural configurations for each composition. To avoid classification based solely on adsorption energy, a global CO_2 activation index was developed and defined as $IACO_2 = z(AG) + z(CTCO_2) + z(Bending) + z(\Delta r\text{C–O})$. In this index, $AG = -\Delta G_{ads}$, $CT_{CO2} = -q\text{CO}_2$, bending corresponds to $(180^\circ - \angle\text{O–C–O})$, and $(\Delta r\text{C–O})$ represents the average elongation of the C–O bonds. This descriptor enabled distinguishing complexes that only stabilize CO_2 from those that induce effective geometric and electronic activation. Although 5IV and 3IV exhibited favorable adsorption, with (ΔG_{ads}) values of -52.978 and -53.494 kcal mol^{-1}, respectively, their molecular activation was low, with nearly linear CO_2 and minimal or unfavorable charge transfer. In contrast, 7III and 7II showed the highest activation, with CT_{CO2} values of 1.206 and 1.163, bending values of 69.867° and 68.869°, and C–O elongations of 0.208 and 0.195 Å, respectively. The standardized ($IACO_2$) ranking identified 7III, 7II, 3III, and 3II as the most relevant systems, with scores of 100.0, 93.8, 88.2, and 86.8, respectively. These results show that CO_2 activation on Cu_nSc nanoclusters should not be assessed solely by (ΔG_{ads}), but rather by a multi-criteria approach that accounts for stability, charge transfer, and molecular distortion.

Keywords: Cu_nSc nanoclusters; CO_2 activation; CO_2 adsorption; r^{2}SCAN-3c; density functional theory; charge transfer; bimetallic clusters; global activation index; molecular bending; C–O bond elongation

Check for updates

Academic Editor: Jiunn Jer Hwang

Received: 2 April 2026
Revised: 27 May 2026
Accepted: 8 June 2026
Published: 10 June 2026

Copyright: © 2026 by the authors. Licensee MDPI, Basel, Switzerland. This article is an open access article distributed under the terms and conditions of the Creative Commons Attribution (CC BY) license.

1. Introduction

The rational design of metal nanoclusters for CO_2 activation requires a detailed understanding of the interdependence between structure, electronic properties, and charge-transfer response. In bimetallic systems, this interdependence is further shaped by synergistic effects, including charge redistribution between metal centers, modifications of the local coordination environment, and changes in the electronic density of states relative to monometallic analogs [1–3]. In this regard, Cu–Sc nanoclusters are an attractive system because the electronic versatility of copper, combined with the low electronegativity

and d-vacancy character of scandium, can generate non-trivial electronic landscapes that favor polarization and partial electron transfer upon interaction with CO_2 [4]. Copper nanoclusters have also been extensively investigated in CO_2-related activation and conversion contexts, including electrochemical CO_2 reduction, and as tunable platforms in other reaction environments where charge redistribution and electronic flexibility are central, motivating their broad exploration in nanoscale reactivity studies [5–8]. At subnanometric scales, quantum-confinement effects lead to discrete electronic levels and a pronounced sensitivity of the electronic response to atomic composition [9–12]. Consequently, heterometallic doping can tune frontier electronic structure and charge redistribution, thereby modulating the extent of CO_2 polarization and the stabilization of partially activated CO_2 adsorption states. Within this focused scenario, incorporating early metals such as scandium into Cu-based clusters is expected to perturb the electronic structure near the Fermi level and enhance polarizability and charge-transfer propensity, making Cu–Sc motifs promising candidates for CO_2 activation, governed by polarization and electron transfer at the adsorption stage.

Such systems are usually studied theoretically by means of density functional theory (DFT) calculations, which enable the access to electronic, energetic, and geometric descriptors that are difficult to isolate experimentally, such as frontier orbital energies, conceptual DFT descriptors, partial charges, adsorption energies, and structural changes induced upon CO_2 binding [13,14]. However, interpreting these descriptors in isolation might lead to inadequate or even misleading findings, especially when adsorption intensity is the only screening criterion. A substantially stabilized CO_2 adduct does not necessarily indicate activation of the CO_2 molecule if the adsorbate remains close to linear, exhibits little charge buildup, and the C–O bond elongation is low. Therefore, a more chemically significant analysis should discriminate between thermodynamic stabilization and molecular activation by incorporating adsorption energy, charge transfer, angular deformation, and C–O bond weakening.

In this study, Cu_nSc nanoclusters with n = 3–7 were looked at as two-metal models for the initial binding and activation of CO_2. This was done using DFT calculations and the r^{2}SCAN-3c method. We looked at four different structural configurations for each makeup, which produced a total of 20 bare clusters, and the Cu_nSc–CO_2 complexes that accompanied them. The descriptions of the separated clusters were used to look at the fundamental electronic features of the catalytic motifs. The adsorption and activation parameters, on the other hand, were taken from the CO_2-bound structures that had been optimized. To avoid ordering the systems solely by their adsorption free energy, a normalized global activation index was created: $IACO_2$ = z (AG) + z ($CTCO_2$) + z ($Bending$) + z (ΔrC–O). Here, $AG = -\Delta G_{ads}$, $CT_{CO2} = -q\mathrm{CO}_2$, $Bending = 180^\circ - \angle$O–C–O, and ΔrC–O is the average lengthening of the C–O bond. This descriptor–response framework was used to determine which Cu_nSc motifs serve only to keep CO_2 stable and which ones actually activate the electronic and geometric structures.

2. Methods

2.1. Model Building and Quantum Computation (DFT)

We have built Cu_nSc bimetallic nanoclusters (n = 3–7) (Figure 1), based on the structural motifs reported earlier for copper nanoclusters, for electrochemical CO_2 reduction. These geometries were selected following the study of Shin et al. [15], who showed with first-principles calculations that the geometry and size of Cu nanoclusters can significantly influence the interaction with CO_2 reduction intermediates and the energy barrier for CHO* -like species formation. In that study, the authors examined Cu_{13}, Cu_{55}, and Cu(111), noting that size and surface geometry can affect electrical stability, the HOMO-LUMO gap,

and adsorbate–metal interactions. Therefore, in the present work, we employed the Cu skeletons as a reference structural platform to introduce a Sc atom and analyze the effect of Cu-Sc polarization on the adsorption and first activation of CO_2.

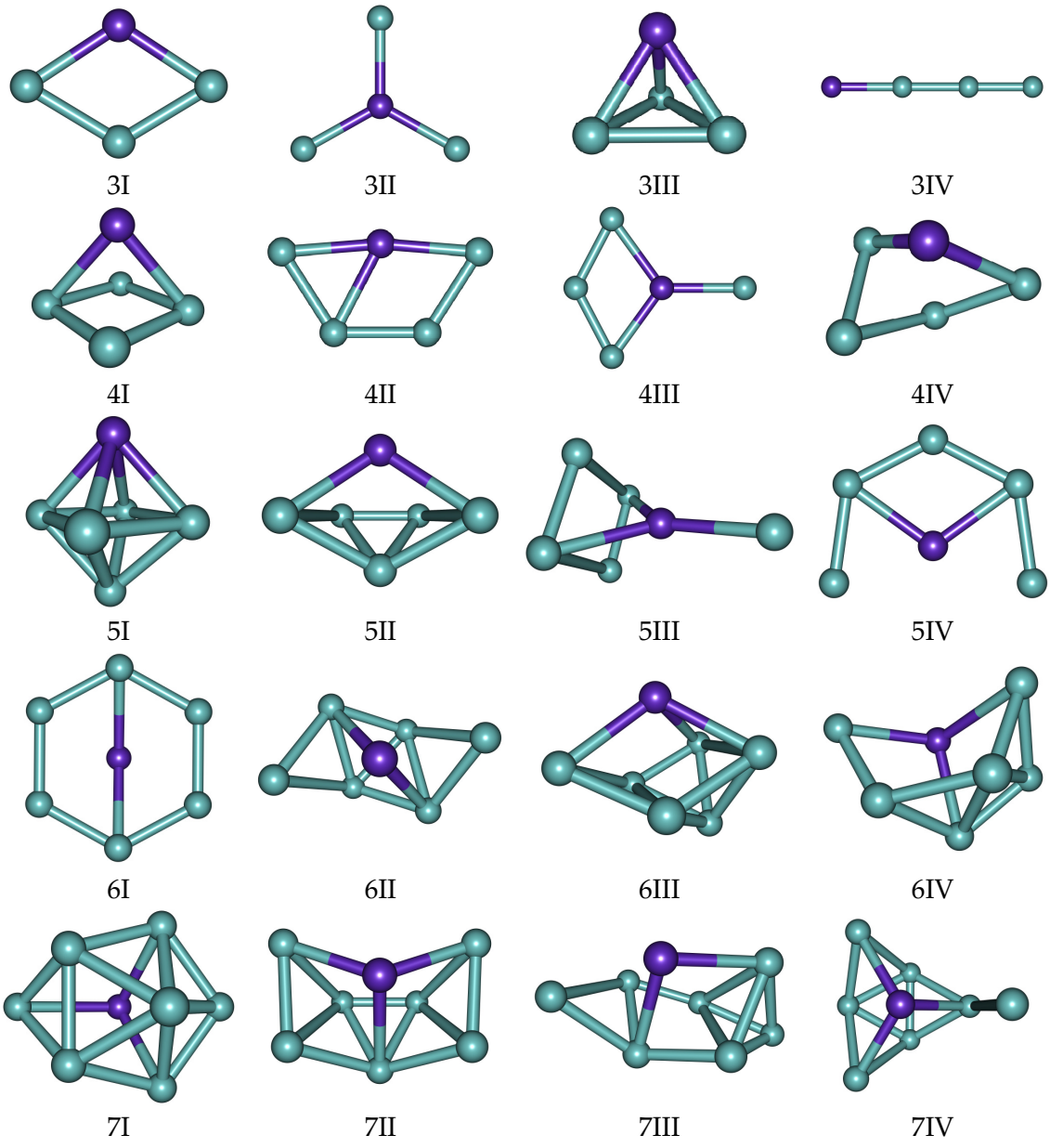


Figure 1. Optimized geometries of free Cu_nSc nanoclusters, with n = 3–7. For each composition, four structural configurations "labeled I–IV" are presented, which are used as initial models to evaluate CO_2 adsorption and activation. The Cu atoms are shown in turquoise, and the Sc atom is shown in violet.

Four structural configurations, or adsorption motifs (I, II, III, and IV), were considered for each Cu_nSc mixture. We studied 20 free clusters and the corresponding Cu_nSc-CO_2 complexes. This selection is not meant as an exhaustive global search over all possible minima of the potential energy surface, but rather as a comparative series of structural motifs based on chemically reasonable metallic geometries, to establish descriptor–response relationships between the electronic structure of the free cluster and the response of the adsorbed CO_2.

2.2. DFT Calculation Details

All electronic-structure computations were carried out using ORCA v6.1.0 software with the r2SCAN-3c composite approach. ORCA is a broad-purpose quantum chemistry package commonly used for DFT calculations, ab initio approaches, molecular characterization, and spectroscopic analysis [16]. The r2SCAN-3c is a composite approach based on the r2SCAN meta-GGA functional, with an optimized triple-ζ basis, a D4 scattering correction, and a gCP counterweight geometric correction to reduce errors arising from basis overlap [17]. This technique was devised to provide an effective description of geometries, thermochemistry, and non-covalent interactions at a reasonably low computational cost.

The geometries of the free Cu_nSc clusters, isolated CO_2 molecule, and Cu_nSc–CO_2 complexes have been optimized without any geometric limitations. Vibrational frequency calculations at the same level of theory were then performed to confirm that the structures correspond to the local minima of the potential energy. The lack of imaginary frequencies was used as the criterion for structural confirmation. The enthalpies and Gibbs free energies of each species were obtained from vibrational calculations using thermochemical adjustments.

CO_2 adsorption was evaluated by comparing the energy of the optimized complex with the sum of the energies of the free cluster and the isolated CO_2. The adsorption energy was calculated as:

$$\Delta E_{ads} = E_{Cu_nSc-CO_2} - E_{Cu_nSc} - E_{CO_2} \quad (1)$$

where $E_{CunSc-CO2}$ corresponds to the total energy of the adsorbed complex, E_{CunSc} to the energy of the free cluster, and E_{CO2} to the energy of the isolated CO_2 molecule.

Similarly, the free energy of adsorption was calculated as:

$$\Delta G_{ads} = G_{Cu_nSc-CO_2} - G_{Cu_nSc} - G_{CO_2} \quad (2)$$

where $G_{CunSc-CO2}$, G_{CunSc}, and G_{CO2} represent the Gibbs free energies of the complex, the free cluster, and isolated CO_2, respectively. To facilitate graphical interpretation, positive quantities associated with the adsorption force were defined as:

$$AE = -\Delta E_{ads} \quad (3)$$

$$AG = -\Delta G_{ads} \quad (4)$$

Thus, higher values of AE or AG indicate more favorable adsorption.

2.3. Free Cluster Electronic Descriptors

The global electronic descriptors of the free Cu_nSc clusters were determined before CO_2 adsorption. This methodological approach allows us to verify whether the intrinsic characteristics of the catalyst can be linked to the subsequent response of the adsorbed CO_2. The HOMO and LUMO energies were obtained directly from the electronic calculations, and the bandgap was determined as:

$$\Delta E_{gap} = \varepsilon_{LUMO} - \varepsilon_{HOMO} \quad (5)$$

Based on this gap, the conceptual DFT descriptors were calculated. The chemical hardness was estimated as:

$$\eta = \frac{\varepsilon_{LUMO} - \varepsilon_{HOMO}}{2} = \frac{\Delta E_{gap}}{2} \quad (6)$$

The chemical softness was calculated as:

$$S = \frac{1}{2\eta} = \frac{1}{\Delta E_{gap}} \tag{7}$$

The electron chemical potential was defined as:

$$\mu = \frac{\varepsilon_{HOMO} + \varepsilon_{LUMO}}{2} \tag{8}$$

and the overall electrophilicity index as:

$$\omega = \frac{\mu^2}{2\eta} \tag{9}$$

The global descriptors were complemented with local charge descriptors derived from natural population analysis (NPA). For each free cluster, the scandium atom charge, q_{Sc}, the average copper atom charge, q_{Cu}, the maximum positive charge, q_{max}, the maximum negative charge, q_{min}, and the Cu–Sc charge separation were obtained:

$$q_{Cu} = \frac{1}{N_{Cu}} \sum_{i=1}^{N_{Cu}} q_{Cu,i} \tag{10}$$

$$\Delta q_{Cu-Sc} = |q_{Sc} - q_{Cu}| \tag{11}$$

This last descriptor was used as a measure of the internal electronic polarization of the bimetallic cluster.

2.4. CO_2 Adsorption and Activation Parameters

CO_2 activation was not evaluated solely based on ΔE_{ads} or ΔG_{ads}, since strong adsorption does not necessarily imply a weakening of the molecule. Therefore, electronic and geometric descriptors specific to the adsorbed carbon dioxide were calculated.

The net charge of the CO_2 fragment was determined by summing the non-shared electron charges (NPA) of the carbon and the two oxygen atoms.

$$q_{CO_2} = q_C + q_{O1} + q_{O2} \tag{12}$$

The shift in emissions toward CO_2 was defined as:

$$CT_{CO_2} = -q_{CO_2} \tag{13}$$

Under this convention, positive CT_{CO2} values indicate an accumulation of electron density on the adsorbed CO_2.

The electronic asymmetry between the two oxygen atoms was calculated as:

$$\Delta q_O = |q_{O1} - q_{O2}| \tag{14}$$

The angular deformation of CO_2 was quantified using:

$$Bending = 180^\circ - \angle O - C - O \tag{15}$$

Therefore, values close to zero indicate nearly linear CO_2, while high values reflect significant molecular bending.

The average elongation of the C–O bonds was calculated as:

$$\Delta r_{C-O} = \frac{(r_{C-O1} - r_0) + (r_{C-O2} - r_0)}{2} \quad (16)$$

where r_0 corresponds to the C–O bond length of free CO_2 optimized at the same theoretical level. Positive values of Δr_{C-O} indicate elongation of the C–O bonds and, therefore, a partial weakening of the linear structure of CO_2. The shortest metal–oxygen distance, d_{M-O}, was also recorded as an auxiliary geometric descriptor of the coordination mode.

2.5. Descriptor–Response Matrix and Overall Activation Index

To prevent a self-referential interpretation based solely on the properties of the free cluster, a descriptor–response matrix was developed. In this matrix, the variables of the free cluster were treated as structural and electronic predictors, while those of the Cu_nSc–CO_2 complex were classified as adsorption and activation responses.

The descriptor block for the free cluster included the following: ΔE_{gap}, S, μ, q_{Sc}, q_{Cu}, $\Delta q_{Cu\text{-}Sc}$. The response section included: AE, AG, CT_{CO2}, ΔqO, bending, Δr_{C-O}, d_{M-O}.

The correlations between the two groups were calculated using Pearson's correlation coefficient:

$$r_{xy} = \frac{\sum_i (x_i - \overline{x})(y_i - \overline{y})}{\sqrt{\sum_i (x_i - \overline{x})^2 \sum_i (y_i - \overline{y})^2}} \quad (17)$$

Pearson's correlation coefficient was used as a descriptive tool to identify linear trends between the properties of the free cluster and the responses of adsorbed CO_2.

Additionally, a global CO_2 activation index, termed IA_{CO2}, was developed, which integrates four variables: free adsorption strength, charge transfer, molecular bending, and C–O elongation. Each of these variables was normalized using standard scores:

$$z(x) = \frac{x - \overline{x}}{s_x} \quad (18)$$

where $\overline{x}$ is the mean, and s_x is the standard deviation of the variable across the entire set of 20 systems.

The overall index was defined as:

$$IA_{CO_2} = z(AG) + z(CT_{CO_2}) + z(Bending) + z(\Delta r_{C-O}) \quad (19)$$

Finally, to simplify the visual comparison, it was normalized on a scale of 0 to 100:

$$IA_{CO_2}^{0-100} = 100\left[\frac{IA_{CO_2} - IA_{min}}{IA_{max} - IA_{min}}\right] \quad (20)$$

In the evaluated series, IA_{min} and IA_{max} denote the minimum and maximum values of the index.

3. Results and Discussion

3.1. Structural Models and Electronic Descriptors of Free Cu_nSc Clusters

Figure 1 illustrates the optimized geometries of free Cu_nSc nanoclusters, with n = 3–7. Four structural configurations, categorized as I–IV, were considered to examine how cluster size and local Cu–Sc topology affect the initial electronic structure before interaction with CO_2. This distinction is methodologically significant because the electronic descriptors of the free cluster were treated as intrinsic variables of the catalytic system. In contrast, the adsorption and activation parameters were determined exclusively after formation of the Cu_nSc–CO_2 complex.

As summarized in Table 1, the free clusters exhibited significant variations in HOMO/LUMO energies, the HOMO–LUMO gap, the descriptors obtained from conceptual DFT, and the NPA charge distribution. The difference in the electronic gap across the various configurations shows that the electronic response of the clusters depends not only on composition but also on the position of the Sc atom in the Cu lattice. Systems with a low gap, such as 3IV and 7II, indicate a relatively greater ease of electronic reorganization; however, subsequent results reveal that this condition is not sufficient to determine the effective activation of CO_2 because it also depends on how it is locally coordinated, on induced charge transfer, and on the geometric deformation of the adsorbate.

Table 1. Descriptors for the free clusters.

Composition	System	HOMO	LUMO	ΔE_{gap}	η	S	μ	ω	qSc	Average qCu	qmax	qmin	ΔqCu–Sc
Cu_3Sc	3I	−3.621	−2.868	0.753	0.376	0.188	−5.055	33.935	0.502	−0.167	0.502	−0.226	0.670
	3II	−4.822	−2.913	1.909	0.955	0.477	−6.279	20.649	0.919	−0.306	0.919	−0.307	1.226
	3III	−3.476	−2.883	0.593	0.297	0.148	−4.918	40.764	0.862	−0.287	0.862	−0.288	1.149
	3IV	−3.925	−3.717	0.207	0.104	0.052	−5.783	161.208	0.296	−0.099	0.296	−0.242	0.395
Cu_4Sc	4I	−3.402	−2.581	0.822	0.411	0.205	−4.693	26.803	0.395	−0.099	0.395	−0.099	0.494
	4II	−3.847	−3.240	0.606	0.303	0.152	−5.467	49.304	0.603	−0.151	0.603	−0.203	0.753
	4III	−3.796	−2.797	1.000	0.500	0.250	−5.195	26.991	0.666	−0.167	0.666	−0.286	0.833
	4IV	−3.763	−2.755	1.008	0.504	0.252	−5.141	26.214	0.496	−0.124	0.496	−0.194	0.620
Cu_5Sc	5I	−3.841	−2.784	1.057	0.528	0.264	−5.233	25.915	0.268	−0.054	0.268	−0.127	0.322
	5II	−4.222	−3.203	1.020	0.510	0.255	−5.824	33.269	0.239	−0.048	0.239	−0.190	0.287
	5III	−3.839	−3.149	0.690	0.345	0.172	−5.413	42.482	0.723	−0.145	0.723	−0.249	0.868
	5IV	−4.456	−3.022	1.433	0.717	0.358	−5.967	24.839	0.558	−0.112	0.558	−0.233	0.669
Cu_6Sc	6I	−3.943	−2.616	1.327	0.664	0.332	−5.251	20.773	0.309	−0.051	0.309	−0.099	0.360
	6II	−3.525	−2.736	0.789	0.395	0.197	−4.893	30.330	0.274	−0.046	0.274	−0.084	0.320
	6III	−3.462	−2.858	0.604	0.302	0.151	−4.891	39.602	0.184	−0.031	0.184	−0.059	0.214
	6IV	−3.673	−2.839	0.834	0.417	0.209	−5.092	31.085	0.293	−0.049	0.293	−0.142	0.341
Cu_7Sc	7I	−3.776	−2.987	0.789	0.395	0.197	−5.270	35.189	−0.067	0.010	0.150	−0.114	0.077
	7II	−3.566	−3.228	0.337	0.169	0.084	−5.180	79.529	0.241	−0.034	0.241	−0.154	0.276
	7III	−4.002	−3.331	0.671	0.336	0.168	−5.668	47.851	0.200	−0.029	0.200	−0.238	0.228
	7IV	−3.603	−3.071	0.532	0.266	0.133	−5.138	49.608	0.103	−0.015	0.108	−0.178	0.118

The charge descriptors shown in Table 1 generally indicated Cu–Sc electronic polarization. In most clusters, a positive NPA charge was observed on the Sc atom, while the Cu atoms had an average negative charge or a charge close to zero. This internal charge separation within the bimetallic cluster is represented by the $\Delta q_{Cu–Sc}$ descriptor. The highest values were 1.226, 1.149, 0.868, and 0.833 for $\Delta q_{Cu–Sc}$ in the cases of 3II, 3III, 5III, and 4III, respectively. These systems are the free clusters with the highest polarization in the entire series.

The above trend confirms that electronic polarization is not controlled exclusively by the number of Cu atoms, but rather by the local topology of the Sc center. In particular, the Cu_3Sc family exhibited a particularly pronounced charge separation in the 3II and 3III configurations, indicating that certain compact arrangements promote a more intense electronic redistribution between Sc and the Cu environment. In contrast, the Cu_7Sc family generally exhibited lower polarization. The 7I case was particularly notable, as Sc exhibited a slightly negative charge and the Cu average was slightly positive, reversing the pattern observed in most systems. This reversal suggests that in larger clusters, the local coordination environment can significantly modify the flow of electron density within the metallic aggregate.

3.2. Multivariate Dataset and Descriptive Statistics of the Descriptors

Figure 2 presents the optimized geometries of the $Cu_nSc–CO_2$ complexes and illustrates how CO_2 adsorbs onto each nanocluster studied. This figure enables qualitative identification of significant differences in the orientation of the adsorbate, the metal atom

or site involved in the interaction, and the degree of structural deformation induced in the CO_2 molecule.

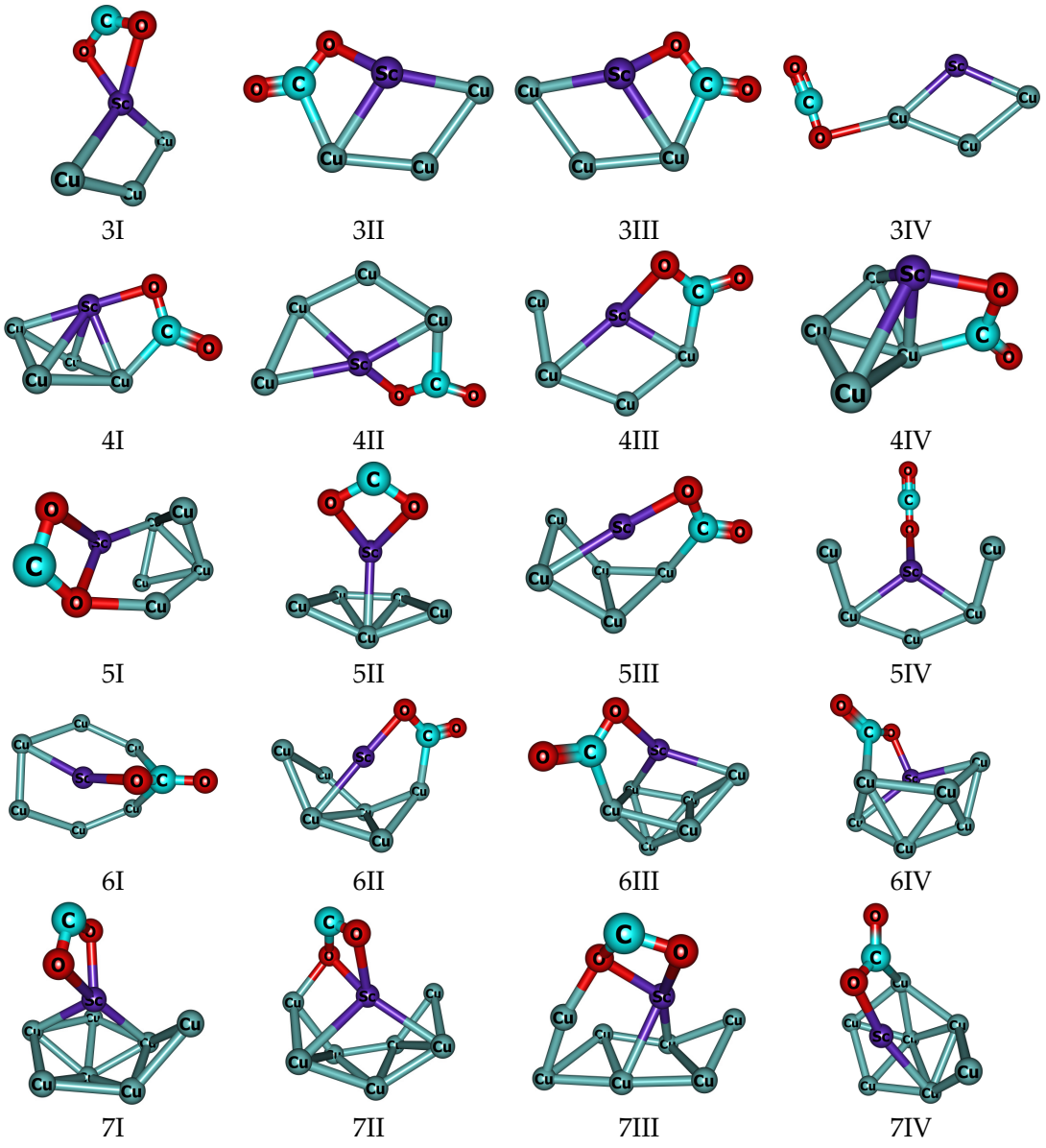


Figure 2. Optimized geometries of the $Cu_nSc–CO_2$ complexes with n = 3–7. For each composition, four adsorption configurations labeled I–IV are shown. Cu atoms are represented in turquoise, Sc atoms in violet, carbon atoms in cyan, and oxygen atoms in red.

An initial examination of Figure 2 shows that not all complexes exhibit the same structural behavior after adsorption. In some systems, CO_2 retains a nearly linear shape and interacts with the cluster in a relatively simple manner. However, in others, a greater angular tilt is observed, along with more uneven coordination. This visual difference is important because CO_2 activation is related not only to the stability of the complex but also to charge transfer to the adsorbate, the curvature of the O–C–O angle, and weakening of the C–O bonds.

Table 2 presents data on adsorption and activation for the optimized complexes: ΔE_{ads}, ΔG_{ads}, charge transfer to the adsorbate, the O–C–O angle, C–O bond elongation, metal–adsorbate distances, and NPA charges of the CO_2 fragment. In this context, integrating the structural information from Figure 2 with the quantitative descriptors in Table 2 clearly

distinguishes between adsorption and molecular activation. The former refers to how the complex is energetically stabilized, while the latter also involves changes in the electronic structure and shape of the CO_2 molecule. This is evident from the accumulation of charge, the bending of angles, and the elongation of C–O bonds.

Table 2. Adsorption and activation of CO_2.

System	ΔE_{ads} (kcal mol^{-1})	ΔG_{ads} (kcal mol^{-1})	qC	qO1	qO2	qCO$_2$	ΔqO	∠O–C–O	rC–O1	rC–O2	ΔrC–O	dM–O
3I + CO_2	−34.728	−25.934	0.697	−0.682	−0.681	−0.666	0.000	126.509	1.255	1.256	0.092	2.161
3II + CO_2	−62.785	−51.923	0.315	−0.552	−0.742	−0.978	0.190	126.191	1.212	1.349	0.117	1.949
3III + CO_2	−64.427	−54.101	0.316	−0.551	−0.743	−0.978	0.191	126.114	1.211	1.349	0.117	1.949
3IV + CO_2	−60.400	−53.494	0.943	−0.451	−0.514	−0.023	0.063	176.511	1.161	1.172	0.003	2.509
4I + CO_2	−44.393	−35.694	0.397	−0.742	−0.540	−0.885	0.202	128.818	1.320	1.211	0.102	1.994
4II + CO_2	−44.880	−35.529	0.354	−0.544	−0.733	−0.923	0.188	127.786	1.213	1.326	0.106	1.985
4III + CO_2	−52.270	−42.988	0.354	−0.545	−0.733	−0.923	0.188	127.763	1.213	1.326	0.106	1.984
4IV + CO_2	−58.527	−47.476	0.370	−0.556	−0.747	−0.933	0.190	126.719	1.210	1.334	0.108	1.958
5I + CO_2	−10.380	−0.683	0.483	−0.731	−0.840	−1.089	0.109	114.380	1.301	1.353	0.164	2.037
5II + CO_2	−16.209	−7.492	0.471	−0.745	−0.745	−1.018	0.001	116.197	1.329	1.328	0.165	2.010
5III + CO_2	−24.758	−15.450	0.378	−0.735	−0.553	−0.910	0.183	128.019	1.325	1.213	0.106	1.992
5IV + CO_2	−64.376	−52.978	1.008	−0.538	−0.401	0.069	0.136	178.445	1.173	1.152	−0.001	2.319
6I + CO_2	−33.079	−23.945	0.334	−0.715	−0.557	−0.937	0.158	127.926	1.319	1.218	0.105	2.029
6II + CO_2	−38.472	−28.479	0.391	−0.543	−0.722	−0.874	0.179	128.620	1.214	1.317	0.102	2.009
6III + CO_2	−41.217	−32.013	0.386	−0.549	−0.726	−0.889	0.177	128.123	1.213	1.324	0.105	1.988
6IV + CO_2	−44.157	−33.544	0.428	−0.711	−0.547	−0.830	0.164	128.916	1.316	1.316	0.152	2.000
7I + CO_2	−20.549	−10.332	0.499	−0.706	−0.702	−0.909	0.004	116.966	1.319	1.322	0.157	2.014
7II + CO_2	−23.590	−13.922	0.453	−0.895	−0.721	−1.163	0.173	111.131	1.424	1.292	0.195	2.042
7III + CO_2	−26.425	−16.572	0.472	−0.963	−0.715	−1.206	0.248	110.133	1.471	1.271	0.208	2.025
7IV + CO_2	−56.513	−45.668	0.406	−0.709	−0.562	−0.865	0.147	127.745	1.325	1.215	0.106	1.996

The most favorable ΔG_{ads} values were observed for 3III, 3IV, 5IV, 3II, 4IV, and 7IV, with values of −54.101, −53.494, −52.978, −51.923, −47.476, and −45.668 kcal mol^{-1}, respectively. If we limit ourselves to the analysis of adsorption free energy, these systems could be considered the best candidates. However, the geometric and electronic descriptors of adsorbed CO_2 demonstrate that strong thermodynamic stabilization does not necessarily imply molecular activation.

This difference is well illustrated by the 5IV + CO_2 system. Despite exhibiting very favorable adsorption,

$$\Delta E_{ads} = -64.376 \text{ kcal mol}^{-1};\ \Delta G_{ads} = -52.978 \text{ kcal mol}^{-1}$$

The adsorbed CO_2 retained a nearly linear geometry, with:

$$\angle O - C - O = 178.445^{\circ};\ Bending = 1.555^{\circ}$$

In addition, the net charge of the CO_2 fragment was positive: +0.069, which leads to a charge transfer defined as:

$$CT_{CO2} = -q_{CO2} = -0.069$$

This value indicates that there is no net accumulation of electron density on the CO_2 molecule. Furthermore, the average elongation of the C–O bonds was practically negligible (−0.001 Å). Therefore, 5IV should be understood as a strong adsorption system, albeit one with restricted geometric and electronic activation.

A similar behavior was observed for 3IV + CO_2, a complex that also exhibited a highly favorable adsorption free energy, with ΔG_{ads} = −53.494 kcal mol^{-1}. However, this thermodynamic stabilization was not accompanied by the significant molecular activation

of CO_2. In this case, the adsorbed molecule maintained a nearly linear geometry, with an ∠O–C–O angle of 176.511° and a bending value of only 3.489°. On the other hand, charge transfer to CO_2 was very low ($CTCO_2$ = 0.023), and the average elongation of the C–O bonds was very small (Δ*r*C–O = 0.003 Å). These results, combined with the behavior observed for 5IV + CO_2, show that both systems thermodynamically stabilize CO_2, but do not induce sufficient electronic redistribution or geometric deformation to be considered activated complexes. Therefore, adsorption energy should not be used as the sole criterion for selecting active systems toward CO_2, as it may overestimate the performance of configurations that act primarily as stabilization or capture sites rather than as true molecular activation centers.

3.3. Systems with Greater Electronic and Geometric Activation of CO_2

Unlike the 3IV and 5IV systems, the 7III + CO_2 and 7II + CO_2 complexes exhibited the highest levels of electronic and geometric activation of CO_2 within the series studied. For 7III + CO_2, a charge transfer to the adsorbate of CT_{CO2} = 1.206 was obtained, accompanied by a molecular bending of 69.867° and an average elongation of the C–O bonds of Δ*r*C–O = 0.208 Å. Similarly, 7II + CO_2 exhibited CT_{CO2} = 1.163, a bending angle of 68.869°, and a C–O elongation of 0.195 Å. These values reveal a significant accumulation of electrons on the CO_2 fragment, a marked deviation from its linear geometry, and a considerable weakening of the C–O bonds. However, these systems were not the most thermodynamically stable, as their adsorption free energies were $\Delta G_{ads} = -16.572$ kcal mol^{-1} for 7III + CO_2 and $\Delta G_{ads} = -13.922$ kcal mol^{-1} for 7II + CO_2. This combination highlights that systems with greater molecular activation do not necessarily coincide with those exhibiting stronger adsorption, but rather with those capable of inducing effective electronic redistribution and significant structural distortion of CO_2.

In contrast, the 3II + CO_2 and 3III + CO_2 complexes exhibited a more balanced equilibrium between activation and adsorption. In 3III + CO_2, the free energy of adsorption was very favorable, with $\Delta G_{ads} = -54.101$ kcal mol^{-1}; in contrast, the charge transfer to CO_2 reached CT_{CO2} = 0.978, with an average C–O elongation of 0.117 Å and a bending angle of 53.886°. Almost identical behavior was obtained for 3II + CO_2, which showed $\Delta G_{ads} = -51.923$ kcal mol^{-1}, CT_{CO2} = 0.978, a bending angle of 53.809°, and Δ*r*C–O = 0.117 Å. Although these two systems do not optimize charge transfer or angular bending separately, they do manage to combine thermodynamically intense adsorption with significant molecular activation. Therefore, 3II + CO_2 and 3III + CO_2 could be considered balanced candidates, given that they effectively stabilize CO_2 while simultaneously inducing geometric and electronic distortions that promote potential reactivity in the future.

3.4. Descriptor–Response Correlation Between the Free Cluster and the Cu_nSc–CO_2 Complex

A descriptor–response matrix was constructed, as shown in Figure 3, to determine whether the electronic characteristics of the free cluster are related to the behavior of the adsorbed CO_2. The descriptors obtained for the free Cu_nSc clusters, which include ΔE_{gap}, *S*, *μ*, *ω*, *q*Sc, *q*Cu, and Δ*q*Cu–Sc, were correlated in this matrix with the responses calculated for the Cu_nSc–CO_2 complexes: *AE*, *AG*, CT_{CO2}, Δ*q*O, bending, Δ*r*C–O, and *d*M–O. This organization allowed a clear distinction between the intrinsic variables of the cluster prior to adsorption and those arising after interaction with CO_2; thus, a self-referential interpretation of the analysis was avoided.

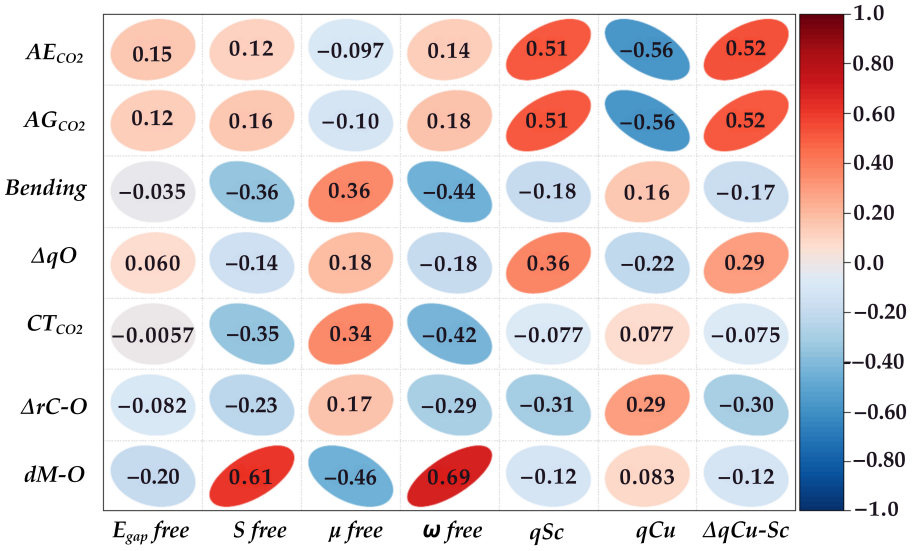


Figure 3. Pearson correlation matrix between the electronic descriptors of the bare Cu_nSc clusters and the adsorption/activation responses of the corresponding Cu_nSc–CO_2 complexes. The horizontal axis contains descriptors of the isolated clusters, whereas the vertical axis contains CO_2 adsorption and activation parameters. Red ellipses indicate positive correlations, while blue ellipses indicate negative correlations.

The correlation matrix revealed that the polarization descriptors of the free cluster are moderately related to the adsorption strengths, as expressed by $AE = -\Delta E_{ads}$ and $AG = -\Delta G_{ads}$. Specifically, AE and AG increased with qSc and ΔqCu–Sc, with correlation coefficients of approximately $r = 0.51$–0.52. Additionally, the two adsorption descriptors showed a negative correlation with qCu, approximately $r = -0.56$. This trend indicates that clusters with a more electropositive Sc center and a more pronounced Cu–Sc charge separation tend to stabilize the adsorbed CO_2 more strongly. From a chemical perspective, this result indicates that the internal polarization of the bimetallic cluster creates electronic spaces that can interact more favorably with the adsorbate.

However, variables directly associated with CO_2 molecular activation, such as CT_{CO2}, bending, and ΔrC–O, did not show strong linear correlations with the global descriptors of the free cluster. This observation is relevant because it shows that the effective activation of CO_2 cannot be explained solely by the HOMO–LUMO gap, smoothness, chemical potential, electrophilicity, or even the Cu–Sc charge separation. In other words, while the polarization of the free cluster contributes to the initial stabilization of CO_2, the actual activation of the adsorbate depends on processes that occur after complex formation, such as the local orientation of the molecule, the coordination mode, the metal–adsorbate distance, and the electronic redistribution induced by the interaction.

The dM–O distance was most strongly correlated with certain global descriptors, including S and ω, suggesting that the cluster's electrophilicity and electronic softness might influence the metal–oxygen distance in the complex. However, this variable was used as an additional geometric descriptor rather than as a direct measure of activation. This is because a shorter M–O distance does not necessarily mean that more charge is transferred, that CO_2 undergoes greater bending, or that the C–O bonds are elongated. Therefore, the activation assessment focused primarily on CT_{CO2}, *bending*, and ΔrC–O, which more directly capture the electronic and structural changes in the adsorbed CO_2.

In summary, Figure 3 indicates that the adsorption and activation of CO_2 depend on partly distinct factors. Adsorption is somewhat related to the electronic polarization already present in Cu–Sc in the free cluster. In contrast, molecular activation is more closely related to the local coordination geometry and the electronic reorganization of the

adsorbed complex. This distinction is important to avoid misinterpreting systems that merely stabilize CO_2 without causing a significant molecular change as being highly active.

3.5. Global CO_2 Activation Index

To combine the stability of the complex and the molecular activation level of CO_2 into a single measure, a global activation index, IA_{CO2} (ec.19), was created based on four additional variables: AG, CT_{CO2}, *bending*, and ΔrC–O. Including these variables simultaneously enabled evaluation not only of the adsorption strength but also of charge transfer to CO_2, the flexing of the O–C–O axis, and the average elongation of the C–O bonds. The normalized index, shown on a scale from 0 to 100, is presented in Figure 4.

$$IA_{CO_2} = z(AG) + z\left(CT_{CO_2}\right) + z(Bending) + z(\Delta r_{C-O})$$

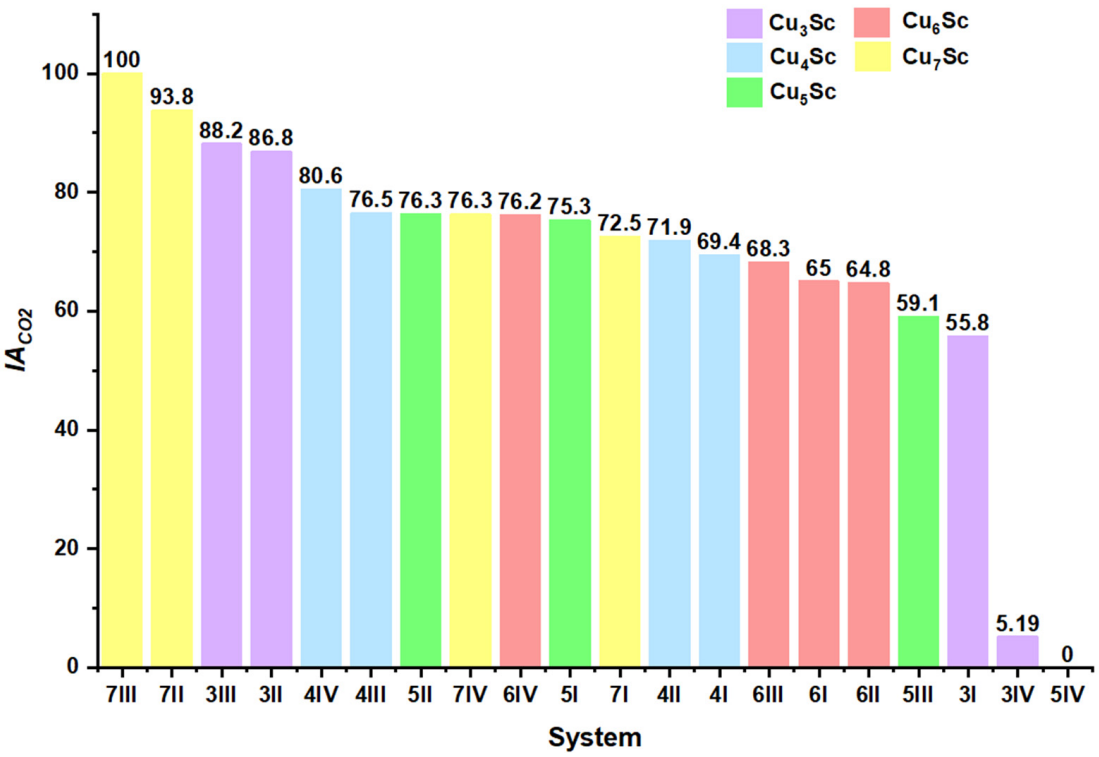


Figure 4. Global CO_2 activation index ranking for Cu_nSc–CO_2 complexes.

The highest IA_{CO2} value was for 7III, with a score of 100.0, followed by 7II, 3III, and 3II, with values of 93.8, 88.2, and 86.8, respectively. These four systems are the most relevant candidates within the evaluated series, although their high ranking stems from different chemical contributions. Systems 7III and 7II stand out primarily for their high charge transfer and the marked angular bending of CO_2, which makes them the complexes with the highest electronic and geometric activations. 3III and 3II, on the other hand, stand out for more balanced behavior, as they combine thermodynamically strong adsorption with appreciable charge transfer, bending, and C–O elongation.

The 4IV, 4III, 5II, 7IV, 6IV, and 5I systems ranked in the middle of the list. These complexes exhibit a certain level of activation, but do not simultaneously maximize all components of the index. Thus, 5I and 5II exhibit significant molecular bending and relatively high charge transfer, but their thermodynamic stabilization is lower than that of the more strongly adsorbed systems. On the other hand, 4IV and 4III exhibited more balanced behavior, with favorable adsorption and moderate activation, making them secondary candidates within the series.

At the bottom of Figure 3 are 3IV and 5IV, with IA_{CO2} values of 5.2 and 0.0, respectively. These two systems are very important to understand because both involve thermodynamically favorable adsorption processes that do not result in significant molecular activation. In particular, their low charge-transfer values, minimal angular bending, and nearly zero elongation of the C–O bonds confirm that CO_2 remains largely unchanged despite being stabilized on the cluster.

The ranking in Figure 4 indicates that CO_2 activity should not be evaluated solely by ΔG_{ads}. If only adsorption free energy was used to make a selection, systems such as 3IV and 5IV could be misclassified as excellent candidates. However, the global index shows that these complexes are primarily cases of strong adsorption with little activation. Therefore, it helps in differentiating between thermodynamic stabilization and actual chemical activation, offering a better tool for prioritizing systems with the highest reaction potential.

3.6. Load-Flex Map for CO_2 Activation

Figure 5 shows the charge–bending activation map for Cu_nSc–CO_2 complexes. In this plot, the horizontal axis shows CT_{CO2}, the vertical axis indicates the molecular bending of CO_2, defined as $180^\circ - \angle$O–C–O, and the size of each bubble is proportional to $AG = -\Delta G_{ads}$. Thus, the figure incorporates three important aspects of the process into a single visual space: electron transfer to the adsorbate, CO_2 deformation, and thermodynamic stabilization of the complex.

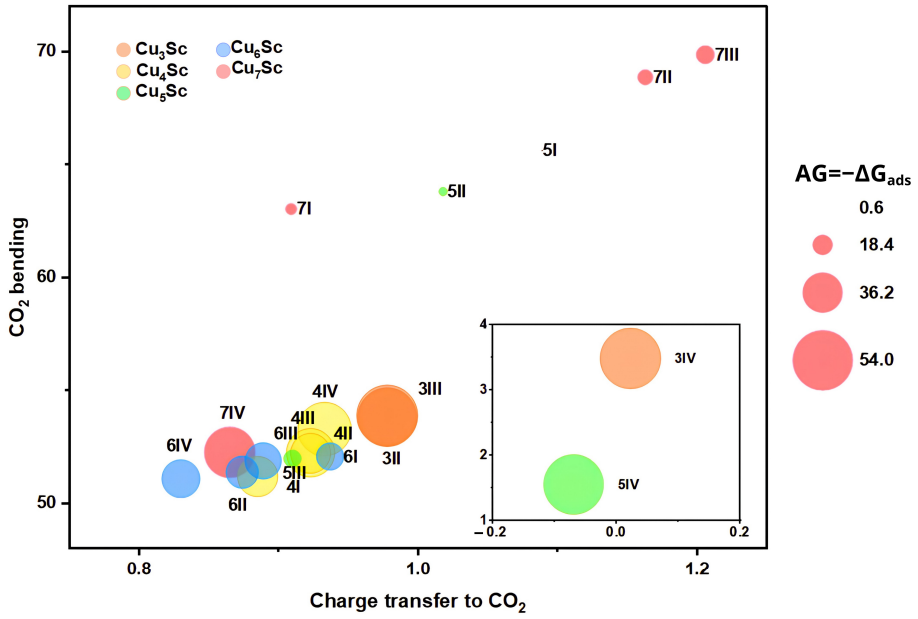


Figure 5. Bubble plot relating charge transfer to CO_2, molecular bending, and adsorption strength in the Cu_nSc–CO_2 complexes. The x-axis represents CT_{CO2}, the y-axis represents CO_2 bending, defined as $180^\circ - \angle$O–C–O, and the bubble size is proportional to $AG = -\Delta G_{ads}$.

The systems in the upper right of the map have the highest charge transfer and the greatest angular bending. In this area, 7III and 7II were primarily found, confirming that these complexes are the main electronic and geometric activators of the series. Although their bubbles are not the largest, their position on the map indicates a strong CO_2 alteration, marked by electron accumulation and a notable deviation from linearity. This response explains their prominent position in the IA_{CO2} ranking.

The 3III and 3II systems were found in a region of high charge transfer and intermediate bending, but with larger bubbles. This suggests that their activity is not due to extreme

geometric activation, but rather to a balance between strong adsorption and significant molecular activation. In practice, these complexes are particularly attractive candidates since they effectively stabilize CO_2 and, at the same time, induce significant electronic redistribution and C–O stretching.

In the central part of the map, systems such as 4IV, 4III, 4II, 6III, 6IV, and 7IV were grouped, exhibiting intermediate charge-transfer and molecular-bending values. The complexes can be defined as moderately activated systems in which CO_2 undergoes a clear electronic and geometric perturbation, though to a lesser extent than in 7III, 7II, 3III, and 3II. The bubble size differs in this region, indicating that thermodynamic stabilization does not always proceed in the same direction as charge transfer or angular bending.

In Figure 5, the inset zooms in on the region of low charge transfer and low molecular bending, where 3IV and 5IV are located. These systems exhibit large bubbles, confirming their high thermodynamic stabilization, but they remain close to the origin of the charge–bending map. This location visually demonstrates that both complexes adsorb CO_2 favorably without inducing significant activation. Thus, the figure directly shows that strong adsorption does not necessarily imply greater activation capacity.

3.7. Local Quantitative Structure–Activation Relationship

In order to further investigate the correlation between the calculated descriptors and the CO_2 activation response, a local quantitative structure–activation analysis was conducted using active-site descriptors obtained from NPA charges and Mayer bond-order data. This analysis was implemented due to the fact that the global descriptors of the bare clusters, while beneficial for the purpose of rationalizing adsorption trends, do not provide a comprehensive explanation for the electronic–geometric activation of the adsorbed CO_2 molecule. Consequently, the model concentrated on the local adsorption site rather than the cluster as a whole (Table 3).

Table 3. Local active-site descriptors and CO_2 activation responses used for the local structure–activation models.

System	Active Site	Δq_{M^*}	$q^{\text{ads-site}}$	I^{Mayer}	CN^{Mayer}	*AG*	$CTCO_2$	Bending	Δr_{C-O}	*ESAI*	D_{A-A}
3I	Sc4	0.399	0.902	0.567	3	25.934	0.666	53.491	0.092	−0.876	−0.550
3II	Sc4/Cu3	0.069	1.265	1.156	3	51.923	0.978	53.809	0.117	0.603	−0.618
3III	Sc4/Cu1	0.127	1.266	1.153	3	54.101	0.978	53.886	0.117	0.607	−0.743
3IV	Cu2	0.149	−0.093	0.050	2	53.494	0.023	3.489	0.003	−7.443	−8.758
4I	Sc5/Cu2	0.431	1.195	0.879	4	35.694	0.885	51.182	0.102	−0.127	−0.382
4II	Sc5/Cu4	0.221	1.154	0.894	4	35.529	0.923	52.214	0.106	0.127	−0.118
4III	Sc5/Cu1	0.157	1.153	0.894	4	42.988	0.923	52.237	0.106	0.129	−0.561
4IV	Sc5/Cu2	0.232	1.115	0.936	4	47.476	0.933	53.281	0.108	0.258	−0.699
5I	Sc6	0.605	0.874	1.134	5	0.683	1.089	65.620	0.164	2.530	4.360
5II	Sc6	0.586	0.825	1.356	5	7.492	1.018	63.803	0.165	2.225	3.649
5III	Sc6/Cu5	−0.043	1.035	1.074	5	15.450	0.910	51.981	0.106	0.074	1.024
5IV	Sc6	−0.095	0.462	0.162	5	52.978	−0.069	1.555	−0.001	−7.918	−9.202
6I	Sc7/Cu2	0.125	0.750	0.864	6	23.945	0.937	52.074	0.105	0.144	0.588
6II	Sc7/Cu4	0.214	0.854	0.878	6	28.479	0.874	51.380	0.102	−0.151	0.024
6III	Sc7/Cu3	0.360	0.898	0.971	6	32.013	0.889	51.877	0.105	−0.017	−0.053
6IV	Sc7/Cu3	0.122	0.791	0.928	6	33.544	0.830	51.084	0.152	0.665	0.538
7I	Sc8	0.352	0.285	1.399	7	10.332	0.909	63.034	0.157	1.685	2.940
7II	Sc8	0.209	0.450	1.188	7	13.922	1.163	68.869	0.195	3.547	4.588
7III	Sc8	0.593	0.793	1.059	7	16.572	1.206	69.867	0.208	3.990	4.873
7IV	Sc8/Cu3	0.104	0.588	1.125	7	45.668	0.865	52.255	0.106	−0.052	−0.901

Here, M* denotes the active metal atom exhibiting the highest total Mayer interaction with the CO_2 fragment.

In each optimized $Cu_nSc–CO_2$ combination, the active site, M*, was taken as the metal atom having the highest total Mayer contact with the CO_2 fragment. If a second metal atom contributes considerably to the CO_2 interaction, the adsorption site is considered a local bimetallic ensemble. The change of the active-site charge for each system was computed as the difference between the NPA charge of the active metal in the adsorbed complex and the NPA charge of the same metal in the corresponding bare cluster.

$$\Delta q_{M^*} = q_{M^*}^{ads} - q_{M^*}^{free} \tag{21}$$

Furthermore, the total Mayer interaction between the active metal site and the CO_2 fragment was employed as a local electronic coupling descriptor, called:

$$I_{M^*-CO_2}^{Mayer}$$

These two descriptors were chosen because they directly explain the local charge redistribution and the electronic connection generated between the metal site and the adsorbed CO_2 molecule.

To characterize the global electronic–structural activation response, an electronic–structural activation index (*ESAI*) was created, excluding the adsorption free energy contribution and considering only the descriptors directly related to CO_2 activation.

$$ESAI = z(CTCO_2) + z(Bending) + z(\Delta r_{C-O}) \tag{22}$$

where CT_{CO2} is the charge transfer to the adsorbate, bending is the angular deformation of CO_2, and Δr_{C-O} is the average C–O bond elongation. In this way, *ESAI* characterizes separately the activation part of the adsorbed molecule from the term of thermodynamic stabilization.

We then created several linear regression models utilizing the normalized local descriptors as predictors. The goal was not to build a classical experimental QSAR model, but to find out how much the local active-site descriptors are able to mimic the calculated CO_2 activation responses for the $Cu_nSc–CO_2$ series. The response variables were the electronic–structural activation index (*ESAI*), the adsorption–activation decoupling descriptor ($D_{A\text{-}A}$) and the individual activation descriptors $CTCO_2$, bending, and $\Delta r_{C\text{-}O}$. Table 4 summarizes the performance of different local structure–activation models.

Table 4. Performance of local structure–activation regression models.

Response	Model Predictors	R^2_{Cal}	R^2_{adj}	R^2_{pred}
ESAI	$z(\Delta q_{M^*}), z\left(I_{M^*-CO_2}^{Mayer}\right)$	0.90	0.84	0.78
$D_{A\text{-}A}$	$z(\Delta q_{M^*}), z\left(I_{M^*-CO_2}^{Mayer}\right)$	0.84	0.83	0.78
CT_{CO2}	$z(\Delta q_{M^*}), z\left(q_{site}^{ads}\right), z\left(I_{M^*-CO_2}^{Mayer}\right)$	0.90	0.84	0.75
Bending	$z(\Delta q_{M^*}), z\left(q_{site}^{ads}\right), z\left(I_{M^*-CO_2}^{Mayer}\right)$	0.90	0.85	0.77
$\Delta r_{C\text{-}O}$	$z\left(CN_{M^*}^{Mayer}\right), z(\Delta q_{M^*}), z\left(I_{M^*-CO_2}^{Mayer}\right)$	0.83	0.80	0.73

The main structure–activation model was obtained by using *ESAI* as the response variable and $z(\Delta q_{M^*})$ and $z\left(I_{M^*-CO_2}^{Mayer}\right)$ as predictors.

$$\widehat{ESAI} = 0.740z(\Delta q_{M^*}) + 2.349z\left(I_{M^*-CO_2}^{Mayer}\right) \tag{23}$$

The model was shown to have good calibration and internal predictive capacity (R^2_{cal} = 0.90, R^2_{adj} = 0.84, R^2_{pred} = 0.78). The very modest discrepancy between R^2_{cal} and

R^2_{pred} indicated that the model was not merely overfitted to the calibration data but also had predictive ability during internal cross-validation (Figure 6). The greater standardized coefficient of $I^{Mayer}_{M^*-CO_2}$ than Δq_{M*} suggests that the activation of CO_2 is dominated by the local electronic coupling between the adsorbate and the active metal site rather than the isolated charge change of the metal atom alone.

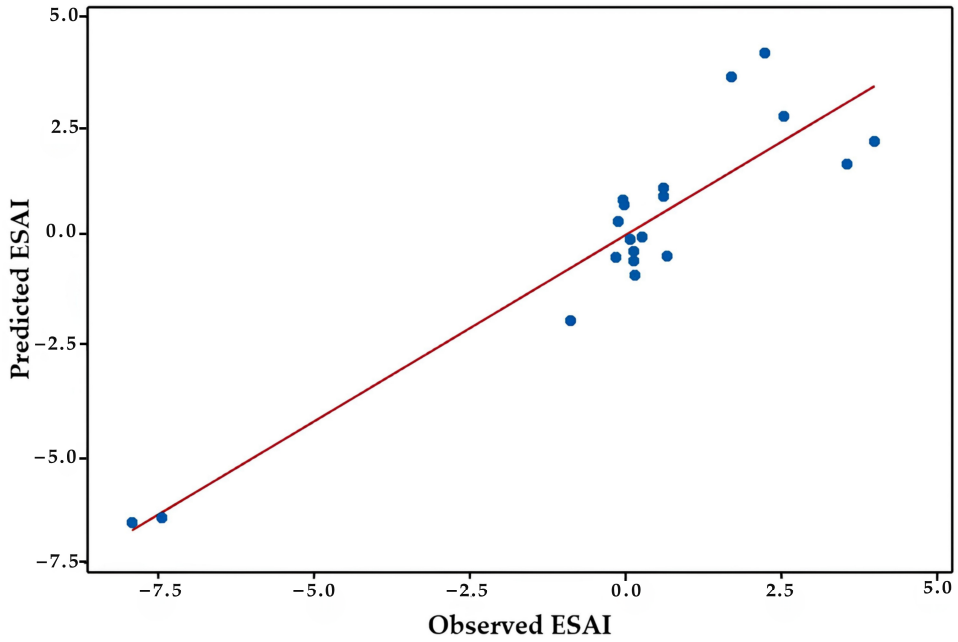


Figure 6. Observed versus predicted *ESAI* values obtained from the local structure–activation model.

As the second model, the adsorption–activation decoupling descriptor, $D_{A-A} = ESAI - z(AG)$, was created. This description divides systems in which electronic–structural activation dominates from those where thermodynamic stabilization is dominant. The equation which resulted was:

$$\widehat{D_{A-A}} = 1.238z(\Delta q_{M^*}) + 2.691z\left(I^{Mayer}_{M^*-CO_2}\right) \quad (24)$$

With R^2_{cal} = 0.84, Q^2_{LOOCV} = 0.78, RMSECV = 1.70, and MAECV = 1.53, this model likewise demonstrated good performance. Thus, whether a particular complex acts as an activation-dominated or adsorption-dominated system is explained by the same local characteristics that explain CO_2 activation.

This conclusion was further reinforced by the individual activation characteristics. With correlation values of 0.90, 0.90, and 0.84, respectively, the local Mayer M^*–CO_2 interaction index demonstrated high positive relationships with $CTCO_2$, bending, and ΔrC−O. These correlations show that the electron accumulation on CO_2, the angular distortion, and the C–O bond elongation all increase with the strength of the local metal–CO_2 electronic interaction. As a result, the Mayer M^*–CO_2 descriptor serves as a concise electronic signature of local CO_2 activation.

4. Discussion

Recent research in computational catalysis, based on descriptors and helped by machine learning, have also tried to tie electronic descriptors to adsorption energy and catalytic tendencies. For instance, Noh et al. utilized non-ab initio descriptors such as d-band width and electronegativity, together with machine learning, to forecast adsorption energies and facilitate large-scale screening of CO_2 reduction catalysts [18]. Their model was able to pre-

dict adsorption energies with good accuracy over a much larger alloy dataset, emphasizing the usefulness of compact descriptors for catalyst identification. Their technique, however, was largely aimed at predicting adsorption energy at high throughput, rather than uncovering the local electrical cause of CO_2 molecule activation. In contrast, the proposed model is active-site-level-based and explicitly correlates the local Mayer M^*-CO_2 interaction and the (Δq_{M^*}) to charge transfer, O–C–O bending, and C–O bond elongation in the Cu_nSc–CO_2 series. Thus, the current dataset is smaller, but the model gives a more chemically precise description of the activation event itself rather than simply the prediction of the adsorption intensity.

Similarly, to forecast adsorption energies across metallic and intermetallic surfaces, Zhang and Cao recently suggested an interpretable deep-learning framework based on local density of states [19]. Compared to the current regression technique, their model is more scalable and generic, particularly for adsorption-energy prediction across extended surfaces. However, the current local structure–activation model is complementary rather than redundant: it finds a compact active-site descriptor, $I^{Mayer}_{M^*-CO_2}$, that quantitatively links local metal–adsorbate coupling with computed CO_2 activation responses, rather than relying solely on electronic-structure representations to predict adsorption energy. Therefore, the benefit of the current model is mechanistic specificity for the Cu_nSc nanocluster family rather than wider transferability. The *ESAI* model achieved $R^2_{cal} = 0.90$ and $Q^2_{LOOCV} = 0.78$, indicating that the dominating activation pattern in this chemically focused dataset is captured by the local electronic coupling descriptor.

In general, these comparisons suggest that the proposed model should not be considered a rival to large-scale machine-learning adsorption-energy models. Instead, it gives a local, DFT-derived structure–activation connection trying to explain why certain Cu_nSc–CO_2 complexes are activation-dominated, adsorption-dominated, or balanced systems. Its key contribution is mechanistic, showing that CO_2 activation in this series of nanoclusters is principally controlled by the local M^*–CO_2 electronic coupling, whereas the adsorption strength alone does not fully capture the activation response.

5. Conclusions

CO_2 adsorption on Cu_nSc nanoclusters was thermodynamically favorable across the evaluated series, but ΔG_{ads} alone was not sufficient to identify effective activating systems. This was evident for 5IV and 3IV, which showed highly favorable adsorption free energies of -52.978 and -53.494 kcal mol^{-1}, respectively, but induced only weak CO_2 activation, with bending values of 1.555° and 3.489°, and nearly negligible C–O elongation. These systems are therefore better described as adsorption-dominated motifs rather than activation-promoting structures.

The strongest electronic–geometric activation was obtained for 7III and 7II, with $CTCO_2$ values of 1.206 and 1.163, bending values of 69.867° and 68.869°, and C–O elongations of 0.208 and 0.195 Å, respectively. In contrast, 3III and 3II provided the best adsorption–activation balance, combining strong ΔG_{ads} values of -54.101 and -51.923 kcal mol^{-1} with $CTCO_2 = 0.978$, bending close to 54°, and $\Delta r_{C-O} = 0.117$ Å.

The descriptor–response analysis showed that adsorption strength is moderately related to the Cu–Sc polarization of the bare cluster, as indicated by the positive correlations of qSc and ΔqCu−Sc with *AE* and *AG* ($r \approx 0.51$–0.52), and the negative correlation with average Cu charge ($r \approx -0.56$). However, CO_2 activation was better explained by local active-site descriptors. The local structure–activation model reproduced *ESAI* using Δq_{M*} and $I^{Mayer}_{M^*-CO_2}$, with $R^2_{cal} = 0.90$ and $Q^2_{LOOCV} = 0.78$, confirming that local metal–CO_2 electronic coupling governs the activation response.

Overall, the $Cu_nSc–CO_2$ systems can be classified into activation-dominated systems, mainly 7III and 7II; balanced adsorption–activation systems, represented by 3III and 3II; and adsorption-dominated systems with weak activation, represented by 3IV and 5IV. Thus, effective CO_2 activation in this series requires not only favorable adsorption, but also strong local $M^*–CO_2$ coupling capable of driving charge transfer, O–C–O bending, and C–O bond elongation.

Author Contributions: Conceptualization, R.O.-T. and J.H.F.; Methodology, K.L.O.P. and J.H.F.; Software, K.L.O.P. and J.H.F.; Validation, K.L.O.P. and J.H.F.; Formal analysis, R.O.-T. and J.H.F.; Investigation, K.L.O.P., R.O.-T. and J.H.F.; Resources, R.O.-T. and J.H.F.; Data curation, J.H.F.;Writing—original draft, K.L.O.P. and J.H.F.; Writing—review and editing, K.L.O.P., R.O.-T. and J.H.F.; Visualization, R.O.-T. and J.H.F.; Supervision, J.H.F.; Project administration, J.H.F.; Funding acquisition, J.H.F. All authors have read and agreed to the published version of the manuscript.

Funding: This research received no external funding.

Data Availability Statement: The original contributions presented in this study are included in the article. Further inquiries can be directed to the corresponding author.

Conflicts of Interest: The authors declare no conflict of interest.

References

1. Muthuperiyanayagam, A.; Nabi, A.G.; Zhao, Q.; Aman-Ur-Rehman; Di Tommaso, D. Adsorption, activation, and conversion of carbon dioxide on small copper–tin nanoclusters. *Phys. Chem. Chem. Phys.* **2023**, *25*, 13429–13441. [CrossRef] [PubMed]
2. Liu, Z.; Li, Y.; Tan, Y.; Zhang, J.; Zhu, Y.; Cao, T.; Lv, H.; Geng, H.; Liu, J.; Zhai, H.; et al. Sulfur-modulated charge-asymmetry Cu–Zn bimetallic nanoclusters for efficient CO_2 electroreduction. *Rare Met.* **2025**, *44*, 6211–6222. [CrossRef]
3. Zhao, R.; Luo, H.; Ouyang, T.; Liu, Z. Boosting Formate Production in Electrocatalytic CO_2 Reduction on Bimetallic Catalysts Enriched with In–Zn Interfaces. *ACS Nano* **2024**, *18*, 35749–35757. [CrossRef] [PubMed]
4. Szalay, M.; Buzsáki, D.; Barabás, J.; Faragó, E.; Janssens, E.; Nyulászi, L.; Höltzl, T. Screening of transition-metal-doped copper clusters for CO_2 activation. *Phys. Chem. Chem. Phys.* **2021**, *23*, 21738–21747. [CrossRef] [PubMed]
5. Baghdasaryan, A.; Bürgi, T. Copper nanoclusters: Designed synthesis, structural diversity, and multiplatform applications. *Nanoscale* **2021**, *13*, 6283–6340. [CrossRef] [PubMed]
6. Wu, Q.; Si, D.; Sun, P.; Dong, Y.; Zheng, S.; Chen, Q.; Ye, S.; Sun, D.; Cao, R.; Huang, Y. Atomically Precise Copper Nanoclusters for Highly Efficient Electroreduction of CO_2 towards Hydrocarbons via Breaking the Coordination Symmetry of Cu Site. *Angew. Chem. Int. Ed.* **2023**, *62*, e202306822. [CrossRef] [PubMed]
7. Ding, M.; Tang, L.; Ma, X.; Song, C.; Wang, S. Effects of ligand tuning and core doping of atomically precise copper nanoclusters on CO_2 electroreduction selectivity. *Commun. Chem.* **2022**, *5*, 172. [CrossRef] [PubMed]
8. Nematulloev, S.; Huang, R.W.; Yin, J.; Shkurenko, A.; Dong, C.; Ghosh, A.; Alamer, B.; Naphade, R.; Hedhili, M.N.; Maity, P.; et al. $[Cu_{15}(PPh_3)_6(PET)_{13}]^{2+}$: A Copper Nanocluster with Crystallization Enhanced Photoluminescence. *Small* **2021**, *17*, e2006839. [CrossRef] [PubMed]
9. Die, D.; Zheng, B.X.; Kuang, X.Y.; Zhao, Z.Q.; Guo, J.J.; Du, Q. Exploration of the Structural, Electronic and Tunable Magnetic Properties of Cu_4M (M = Sc-Ni) Clusters. *Materials* **2017**, *10*, 946. [CrossRef] [PubMed]
10. Srikulwong, U.; Wiwasuku, T.; Puangmali, T. Surface Engineering of Bimetallic Nanoclusters: Ligand–Solvent Interplay for Enhanced Charge Transfer and Optical Modulation. *Langmuir* **2025**, *41*, 16009–16021. [CrossRef] [PubMed]
11. De Lara-Castells, M.P. First-principles modelling of the new generation of subnanometric metal clusters: Recent case studies. *J. Colloid Interface Sci.* **2022**, *612*, 737–759. [CrossRef] [PubMed]
12. Morato-Márquez, J.A.; Torres-Torres, J.G.; Ortíz-Chi, F. DFT Study of Structural, Chemical, and Optical Properties in Cun and PdCun−1 Clusters (n = 3–20). *J. Comput. Chem.* **2025**, *46*, e70183. [CrossRef] [PubMed]
13. Mattsson, M.S.M.; Azens, A.; Niklasson, G.A.; Granqvist, C.G.; Purans, J. Li intercalation in transparent Ti–Ce oxide films: Energetics and ion dynamics. *J. Appl. Phys.* **1997**, *81*, 6432–6437. [CrossRef]
14. Hada, A.M.; Lamy de la Chapelle, M.; Focsan, M.; Astilean, S. Recent advances in metal nanoclusters: From novel synthesis to emerging applications. *Molecules* **2025**, *30*, 3848. [CrossRef] [PubMed]
15. Shin, D.Y.; Won, J.S.; Kwon, J.A.; Kim, M.; Lim, D. First-principles study of copper nanoclusters for enhanced electrochemical CO_2 reduction to CH_4. *Comput. Theor. Chem.* **2017**, *1120*, 84–90. [CrossRef]
16. Neese, F.; Wennmohs, F.; Becker, U.; Riplinger, C. The ORCA quantum chemistry program package. *J. Chem. Phys.* **2020**, *152*, 224108. [CrossRef] [PubMed]

17. Grimme, S.; Hansen, A.; Ehlert, S.; Mewes, J. r2SCAN-3c: A "Swiss army knife" composite electronic-structure method. *J. Chem. Phys.* **2021**, *154*, 064103. [CrossRef] [PubMed]
18. Noh, J.; Kim, J.; Back, S.; Jung, Y. Catalyst design using actively learned machine with non-ab initio input features towards CO_2 reduction reactions. *arXiv* **2017**, arXiv:1709.04576. [CrossRef]
19. Zhang, Z.; Cao, X. Orbital-interaction-aware deep learning model for efficient surface chemistry simulations. *arXiv* **2025**, arXiv:2507.20496. [CrossRef]

Disclaimer/Publisher's Note: The statements, opinions and data contained in all publications are solely those of the individual author(s) and contributor(s) and not of MDPI and/or the editor(s). MDPI and/or the editor(s) disclaim responsibility for any injury to people or property resulting from any ideas, methods, instructions or products referred to in the content.